


 Cite this: *RSC Adv.*, 2022, **12**, 23074

# Improving thermoelectric performance by constructing a SnTe/ZnO core–shell structure†

 Song Li,<sup>a</sup> Jingwen Zhang,<sup>\*ab</sup> Dawei Liu,<sup>a</sup> Yan Wang<sup>a</sup> and Jiuxing Zhang<sup>id</sup><sup>\*a</sup>

SnTe is becoming a new research focus as an intermediate temperature thermoelectric material for its environment-friendly property. Herein, the SnTe/ZnO core–shell structure prepared by a facile hydrothermal method is firstly constructed to enhance the thermoelectric performance. The characterization results demonstrate that ZnO nanosheets are coated on the surface of SnTe particles by *in situ* synthesis and converted into ZnO nano-dots by spark plasma sintering. The energy barriers built by the SnTe/ZnO core–shell structure improve the Seebeck coefficient effectively. Additionally, the increased density of interfaces induced by ZnO can effectively scatter low/medium frequency phonons, reducing the lattice thermal conductivity in the low/medium temperature region. Further, the point defects caused by Cu<sub>2</sub>Te-alloying strengthen the scattering of high frequency phonons. The lattice thermal conductivity reaches 0.48 W m<sup>-1</sup> K<sup>-1</sup>, which is close to the amorphous limit of pristine SnTe. As a result, a peak *ZT* value of 0.94 is achieved at 823 K for SnTe(Cu<sub>2</sub>Te)<sub>0.06</sub>–1.5% ZnO, benefiting from the synergistic optimization of thermal and electrical properties. This provides a new idea for exploring an optimization strategy of thermoelectric performance.

 Received 10th July 2022  
 Accepted 9th August 2022

DOI: 10.1039/d2ra04255j

[rsc.li/rsc-advances](https://rsc.li/rsc-advances)

## 1. Introduction

Due to the rising serious problem of environmental pollution and the depletion of non-renewable fossil fuels, the demand for developing and applying new clean energy is desired to be solved. Thermoelectric materials have a function of realizing direct conversion between heat and electricity without any moving parts, noise, or additional emissions.<sup>1–3</sup> Thus, thermoelectric materials are receiving increasing attention for their potential application. The performance of thermoelectrical materials (TE) is expressed by the dimensionless figure of merit  $ZT = S^2\sigma T/\kappa$ , which is decided by three main physical parameters including the Seebeck coefficient, *S*, electrical conductivity,  $\sigma$ , and thermal conductivity,  $\kappa$ .<sup>4,5</sup> So, we expect thermoelectrical materials to achieve a high *ZT* value with the characteristics of a high Seebeck coefficient, high electrical conductivity, and low thermal conductivity.<sup>6</sup>

In the past few decades, intermediate temperature TE materials, such as Sb<sub>2</sub>Si<sub>2</sub>Te<sub>6</sub>,<sup>7</sup> Bi<sub>2</sub>Si<sub>2</sub>Te<sub>6</sub>,<sup>8</sup> GeTe,<sup>9</sup> AgMnSbTe<sub>4</sub>,<sup>10</sup> Mg<sub>3</sub>Sb<sub>2</sub>,<sup>11</sup> and SnSe,<sup>12</sup> have received widespread attention and undergone intensive research for their application prospects. For example, the well-investigated lead telluride (PbTe) based TE materials have obtained high *ZT* values, especially p-type

PbTe.<sup>13–15</sup> However, the toxicity of lead element limits their large-scale applications. SnTe-based TE materials have attracted much interest for their lead-free and environment-friendly characteristics.<sup>2</sup> Moreover, SnTe has a similar rock salt crystal structure and electronic band structure with PbTe.<sup>16,17</sup> Nevertheless, some reasons seriously limit the TE performance of the pristine SnTe: the intrinsic high hole concentration,<sup>18</sup> a small band gap as well as a larger energy separation between the light and heavy valence bands,<sup>19</sup> and the high lattice thermal conductivity.<sup>20</sup>

At present, there is much research on SnTe to optimize the TE performance. The formation of SnTe solid solution with mono-tellurides, such as MgTe,<sup>21</sup> HgTe,<sup>22</sup> CdTe,<sup>6,23</sup> MnTe,<sup>24,25</sup> CaTe<sup>26</sup> can effectively enlarge the band gap to postpone the temperature at which the bipolar effect appears and reduce the separation between light and heavy valence band to realize valence band convergence, which is an effective way to optimize the Seebeck coefficient (*S*) and eventually the power factor ( $S^2\sigma$ ). Moreover, Zhang *et al.* proved that indium alloying can induce resonant state near the valence band of SnTe,<sup>27</sup> which can improve the density of states (DOS) near Fermi level  $E_F$  of SnTe and dramatically improve the *S*, especially at room temperature, realizing the power factor PF of  $\sim 20.3 \mu\text{W cm}^{-1} \text{K}^{-2}$  and *ZT* value of  $\sim 1.1$  at 873 K in In<sub>0.0025</sub>Sn<sub>0.9975</sub>Te.

Besides band engineering, energy filtering effect can also effectively increase the *S* along with PF by strengthening the scattering of energy-relevant carriers.<sup>28,29</sup> Zheng *et al.* demonstrated that the high-temperature solid state reaction can introduce BiCuSeO@SnO<sub>2</sub> core–shell nanostructure into the

<sup>a</sup>School of Materials Science and Engineering, Hefei University of Technology, Hefei 230009, China. E-mail: zjwhfut18205614071@163.com; zjiuxing@hfut.edu.cn

<sup>b</sup>School of Physics and Materials Engineering, Hefei Normal University, Hefei 230061, China

 † Electronic supplementary information (ESI) available. See <https://doi.org/10.1039/d2ra04255j>


SnTe matrix.<sup>30</sup> A mass of heterogeneous interfaces formed not only strengthen the energy filtering effect, decreasing the carrier concentration and increasing the Hall mobility, but also effectively reducing the  $\kappa_1$  and finally improving the TE performance.<sup>31</sup> In our previous work, the PbTe@C core-shell nanostructure was introduced in the SnTe matrix to effectively improve the thermal properties.<sup>32</sup> However, nanopores and amorphous carbon layer can extensively scatter carriers as well, degrading the electronic transport. Thus, this work pretends to replace amorphous carbon layer with ZnO to introduce the energy filtering effect by constructing energy barrier, realizing the improvement of electrical performance.

In this study, a facile hydrothermal method is applied to *in situ* synthesize SnTe/ZnO core-shell particles, followed by spark plasma sintering (SPS) process to prepare bulk samples. We first investigate the TE performance of SnTe- $x\%$  ZnO ( $x = 0, 1, 1.5, 2.5$ ) to obtain the best ZnO content  $x$ , and then investigate the TE properties of the SnTe(Cu<sub>2</sub>Te)<sub>y</sub>-1.5% ZnO ( $y = 0.03, 0.04, 0.05, 0.06$ ) to determine the best component of Cu<sub>2</sub>Te. We reveal that constructing SnTe/ZnO core-shell structure in SnTe matrix can effectively improve the  $S$  through energy filtering effect. Besides, the increased density of interfaces involved by ZnO can effectively scatter the low/medium frequency phonons to reduce the  $\kappa_1$  in the low/medium temperature region. And Cu<sub>2</sub>Te alloying can directly scatter the high frequency phonons and further reduce the  $\kappa_1$  in the high temperature region without serious degradation of electrical performance. Consequently, a peak  $ZT$  value of  $\sim 0.94$  can be obtained for SnTe(Cu<sub>2</sub>Te)<sub>0.06</sub>-1.5% ZnO at 823 K, almost 138% of the pristine SnTe.

## 2. Experiment section

### 2.1. Synthesis of SnTe- $x\%$ ZnO samples

Samples with nominal compositions of SnTe were synthesized by mixing appreciated ratios of high purity tin (99.99%) and tellurium (99.99%) metal granules. Stoichiometric amounts of metal granules were weighed before being loaded in quartz ampoules (20 mm in diameter) which were vacuumed to a pressure below  $10^{-5}$  torr and sealed using oxyhydrogen flame. The sealed tubes were then slowly heated up to 1373 K in a muffle furnace and held at this temperature for 4 h. Afterwards, the ingots were achieved by cooling the tubes in the open air and subsequently crushed into fine powders with the mortar and pestle by hand for one hour.

The decent powders were covered with  $x$  wt% ZnO nanosheets ( $x = 1, 1.5, 2$ ) by *in situ* synthesis with a facile hydrothermal method using ZnCl<sub>2</sub>, C<sub>6</sub>H<sub>12</sub>N<sub>4</sub>, and C<sub>6</sub>H<sub>5</sub>Na<sub>3</sub>O<sub>7</sub> as original materials.

**Synthesis of SnTe/Zn(OH)<sub>2</sub> particles.** First, the hand grinding micro-SnTe powders were dispersed by ultrasonic shock in the deionized water (40 ml) for 20 min. Then, the C<sub>6</sub>H<sub>12</sub>N<sub>4</sub> (0.112 g), C<sub>6</sub>H<sub>5</sub>Na<sub>3</sub>O<sub>7</sub> (0.023 g), and calculated amounts of ZnCl<sub>2</sub> were weighted and added into the dispersed suspension. Afterwards, the prepared suspension was heated at 358 K for 6 h under continuous stirring. Finally, SnTe/Zn(OH)<sub>2</sub> particles were achieved after centrifuging, washing, and drying.

**Synthesis of SnTe- $x\%$  ZnO powders.** The SnTe/Zn(OH)<sub>2</sub> particles were calcined in the tube furnace at 573 K for 1 h under a 5% H<sub>2</sub>/95% Ar flow to obtain the SnTe/ZnO particles. The 1%, 1.5%, and 2.5% SnTe/ZnO composites synthesized with 0.1172 g, 0.1758 g, and 0.2930 g ZnCl<sub>2</sub>.

The final powders were loaded into a graphite model of 20 mm inner diameter with the uniaxial pressure of 50 MPa and sintered at the temperature of 823 K for 5 min by SPS apparatus. Finally, the coin-shape samples with a diameter of 20 mm and thickness of 5 mm were obtained.

### 2.2. Synthesis of SnTe(Cu<sub>2</sub>Te)<sub>y</sub>-1.5% ZnO samples

A similar preparation process was applied to SnTe(Cu<sub>2</sub>Te)<sub>y</sub> alloy powders and high purity cuprum (99.99%) metal powder was used in addition. The process of *in situ* synthesizing 1.5% ZnO nanosheet shell was the same as above.

### 2.3. Material characterization

The information on structure and phase of the prepared samples were obtained with Cu K $\alpha$  radiation ( $\lambda = 0.15418$  nm) on a Rigaku diffractometer accelerated in a  $2\theta$  range of 20–80°. The microstructure investigation on a freshly broken surface of the samples is carried out by scanning electron microscopy (SEM) (SIGMA HV iNote, ZEISS, Germany) and transmission electron microscope (TEM) (Tecnai 20 D550 S-Twin, FEI, Holland). The elemental composition analysis was conducted on the energy dispersive spectrometry (EDS) (Inca, Oxford Instruments). The samples were cut into bars with dimensions of  $2.5 \times 2.5 \times 12$  mm<sup>3</sup> and used to measure the Seebeck coefficient and electrical conductivity simultaneously by operating the commercial LRS-3 Linseis Germany system in a helium atmosphere at the temperature ranging from 323 K to 873 K. The thermal diffusivity ( $\lambda$ ) for the polished samples with  $\sim 12.65$  mm diameter and  $\sim 1.5$  mm thickness was directly measured ranging from 300 K to 873 K by the laser flash diffusivity method in a Netzsch LFA 457. The density of samples ( $d$ ) was determined using the Archimedes method and the specific heat capacity ( $C_p$ ) was substituted by the following formulas:  $C_p = (3.91 \times 10^{-3} \times T + 24.35) \times N_a/M$ ,  $C_{p, \text{composite}} = \sum C_{pi} \times m_i\%$ .<sup>33</sup> The total thermal conductivity  $\kappa$  was calculated from the formula:  $\kappa = \lambda d C_p$ . The carrier concentration ( $n$ ) can be calculated *via* the formula:  $n = 1/(eR_H)$ , where  $R_H$  is the Hall coefficient that measured on Lake Shore 8400 in a magnetic field ranging from  $-0.8$  T to  $0.8$  T, and  $e$  is the elemental charge. The Hall mobility ( $\mu$ ) was computed by  $\mu = \sigma/ne$ .

## 3. Results and discussion

Fig. 1 shows the schematic diagram of synthesis route for SnTe/ZnO core-shell particles. First, the SnTe particles are prepared by conventional melting and hand grinding (Fig. S1†), exhibiting irregular shapes, and the zeta potential test indicates that its surface is negatively charged (Fig. S2†). After that, Zn<sup>2+</sup> ions can be absorbed by the surface of SnTe particles through electrostatic force. With the temperature rising, the Zn ions will gradually hydrolyze and turn into Zn(OH)<sub>2</sub> nanosheets to form



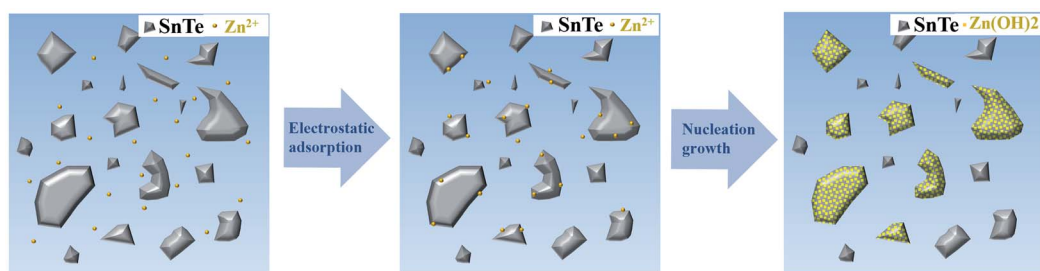


Fig. 1 Schematic diagram of SnTe/ZnO core-shell particles *in situ* synthesis.

SnTe/Zn(OH)<sub>2</sub> composite. Finally, the SnTe/Zn(OH)<sub>2</sub> particles are calcined at 573 K for 1 h to obtain SnTe/ZnO core-shell particles.<sup>34</sup> Fig. 2a displays the XRD pattern of SnTe-*x*% ZnO (*x* = 0, 1, 1.5, 2.5) powders, and the characteristic peaks can be indexed to rock-salt SnTe structure (PDF # 46-1210). Fig. 2b shows the enlarged XRD pattern from 36° to 36.5°, the ZnO peak can be obviously observed.

Fig. 3a displays the low-magnification SEM image of SnTe-1.5% ZnO powders, which shows that the grain size of hand-grinding SnTe particles distributes from dozens of nanometers to dozens of microns. Moreover, due to the low loading fraction of ZnO, the surface of only part of SnTe particles look rough and other SnTe particles are smooth. Thus, two large size particles with smooth and rough surface (Fig. 3b) are selected respectively for EDS characterization. As shown in Fig. 3c and d, EDS results demonstrate that Zn and O elements only exist in area A instead of area B, thus the surface in area A agrees with

ZnO composition well. Besides, the surface of the SnTe particles became rough, which is due to the hydrolyzation of Zn<sup>2+</sup> and subsequent dehydration.<sup>34</sup>

The TEM images of Fig. 4a and b display the SnTe/ZnO core-shell particles, and it can be obviously seen that the SnTe surface was entirely coated with a floccule structure. Fig. 4c shows the HRTEM image along with the thin areas at the edge of the SnTe/ZnO core-shell particles. The lattice fringes with an interplanar spacing of 0.24 nm are the (101) plane of ZnO, indicating that ZnO nanosheets is successfully coated on the surface of SnTe. Thus, the existence of SnTe/ZnO core-shell structure is proved. Fig. 4d shows a high-angle annular dark-field scanning transmission electron microscopy (HAADF-STEM) image of a SnTe/ZnO core-shell particle, with a size of ~4 μm. Moreover, the corresponding EDS mapping results of the SnTe/ZnO core-shell particle (Fig. 4d1-d4) clearly indicated that the Sn, Te, Zn, and O elements are homogeneously distributed, confirming the presence of SnTe/ZnO core-shell structure.

Fig. S3a and b† show the XRD patterns of SnTe-*x*% ZnO (*x* = 0, 1, 1.5, 2.5) bulks, suggesting that ZnO phase still exists in the SnTe matrix after SPS process. In order to characterize the morphology of ZnO nanosheets after SPS process, SEM and EDS are carried out, as shown in Fig. 5. Fig. 5a and b display the gradually magnified SEM images of the fractured of SnTe-1.5% ZnO bulks. It is found that there are many nano-dots with the size of 10–20 nm distributed around the grain boundary of SnTe. Moreover, the nano-dots are aggregated and well-attached to the surface of SnTe grains. To investigate the composition of the nano-dots above, EDS point scanning (Fig. 5c and d) is carried out, clearly indicating the obvious Zn and O peaks only appear in area B. Combining the results of SEM and EDS, it is

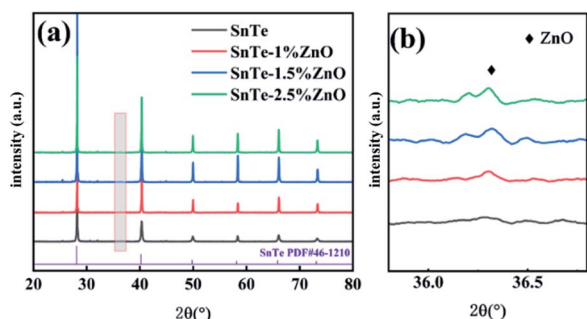


Fig. 2 (a) XRD patterns of SnTe-*x*% ZnO (*x* = 0, 1, 1.5, 2.5) powders. (b)  $2\theta$  shift for SnTe-*x*% ZnO (*x* = 0, 1, 1.5, 2.5) powders.

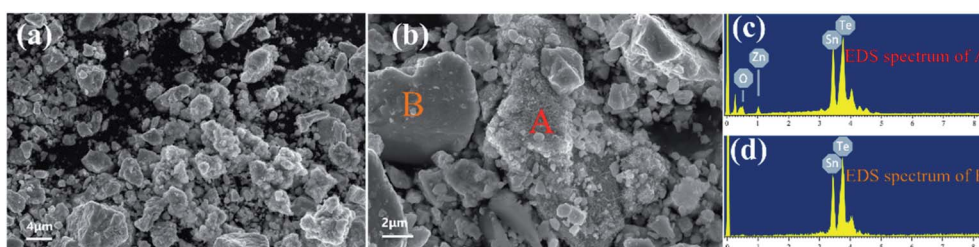


Fig. 3 (a) Low-magnification SEM image of the particles for SnTe-1.5% ZnO powders. (b) High-magnification SEM of the rough and smooth particles. (c and d) EDS spectrum of areas A and B in graph (b), respectively.



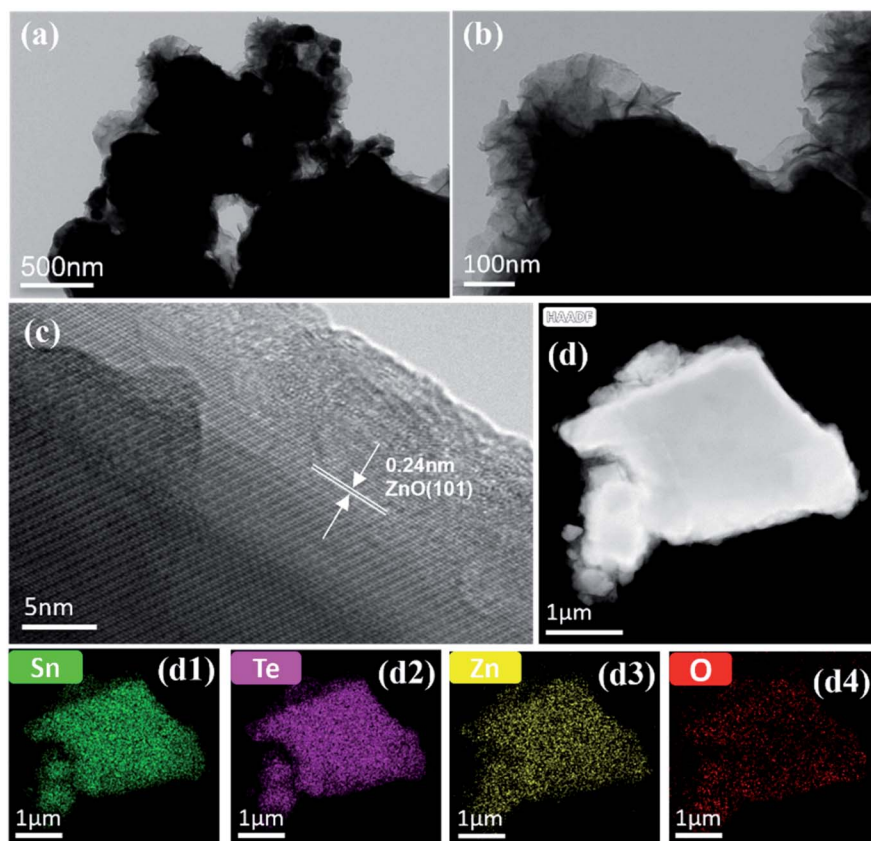


Fig. 4 (a and b) Low and medium magnification TEM images of SnTe/ZnO core-shell particles for SnTe–1.5% ZnO powders. (c) High-resolution TEM (HRTEM) image along with the thin areas at the edge of the SnTe/ZnO core-shell particle. (d) High-angle annular dark-field scanning transmission electron microscopy (HAADF-STEM) image of a SnTe/ZnO core-shell particle. (d1–d4) Elemental energy dispersive spectroscopy (EDS) mapping of graph (d).

speculated that the ZnO nanosheets coated on SnTe grains transform into ZnO nano-dots after SPS process. In the SPS process, the plasma generated by microscopic electrical discharge in the gaps between the powder particles will produce

high temperature at the surface of the particles.<sup>35,36</sup> When the temperature is high enough, the ZnO nanosheets will occur plastic deformation and transform into nanodots under the effect of the surface tension.

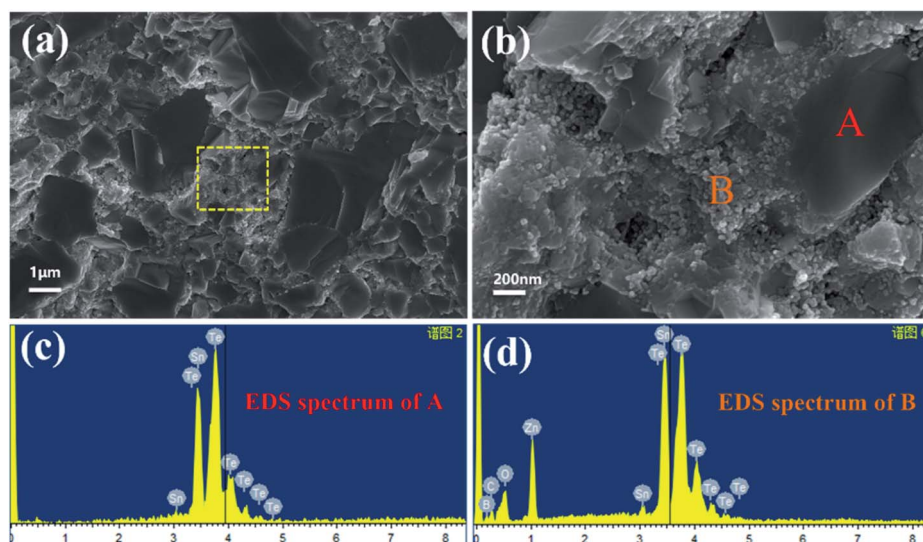


Fig. 5 (a and b) SEM images of the fractured surface of SnTe–1.5% ZnO. (c and d) EDS spectra of areas A and B in graph (b), respectively.



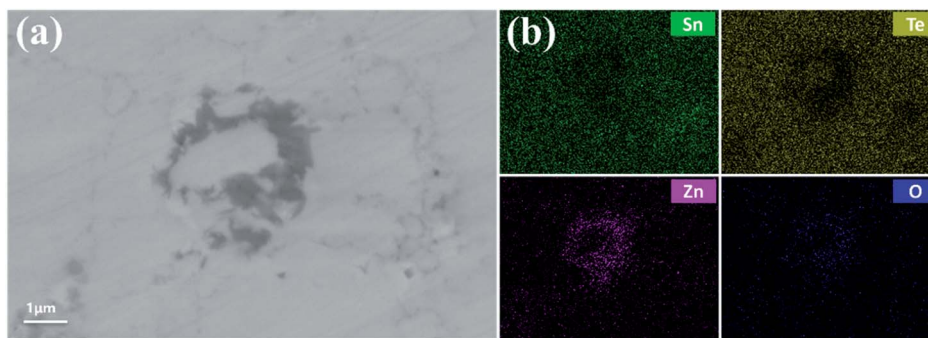


Fig. 6 (a) Backscattering scanning electron (BSE) images of polished surfaces of SnTe–1.5% ZnO (b) EDS mapping of graph (a).

To determine the spatial distribution of the elements, Fig. 6 gives the backscattered electron (BSE) and EDS mapping results on a polished surface of SnTe–1.5% ZnO sample. Fig. 6a clearly displays that the dark phase appears around the grey SnTe grain boundary, with a size of  $\sim 4 \mu\text{m}$ , keeping a typical core–shell structure.<sup>37</sup> The EDS mapping of this area presented in Fig. 6b exhibits the Sn, Te, Zn, and O distribution, respectively. The enrichment regions of bright areas in Zn and O EDS mapping correspond to the dark shell in graph (a), and the bright areas in Sn and Te EDS mapping consist with the grey phase in graph (a) as well. Thus, we can confirm that the composition of the dark shell agrees well with ZnO and the core is SnTe. Therefore, the SnTe/ZnO core–shell still exist after SPS process.

Fig. 7 shows the electrical conductivity  $\sigma$ , Seebeck coefficient  $S$ , power factor PF of SnTe– $x\%$  ZnO ( $x = 0, 1, 1.5, 2.5$ ) bulks. As

can be seen in Fig. 7a, the  $\sigma$  of all the samples experiences a great drop with the increment of temperature, exhibiting the characteristic of degenerate semiconductors. Meanwhile, the  $\sigma$  decreases greatly at the whole temperature region after constructing SnTe/ZnO core–shell structure, which can be explained by the sharp decrease of carrier concentration  $n_{\text{H}}$  in the inset of Fig. 7b. For instance, the  $n$  decreases sharply from  $1.6 \times 10^{20} \text{ cm}^{-3}$  for SnTe to  $0.86 \times 10^{20} \text{ cm}^{-3}$  for SnTe–1% ZnO. To its surprise, the carrier mobility  $\mu$  rises obviously to  $519 \text{ cm}^2 \text{ V}^{-1} \text{ s}^{-1}$  for SnTe–1% ZnO, which is 132.7% higher than pristine SnTe. As shown in the Fig. 7d, due to ZnO is a wide band-gap semiconductor material, the difference of Fermi level, defects, and the lattice mismatch between the ZnO and SnTe form the energy barrier at the SnTe/ZnO heterogeneous interface.<sup>31,38</sup> Such energy barrier will lead to the energy filtering effect by

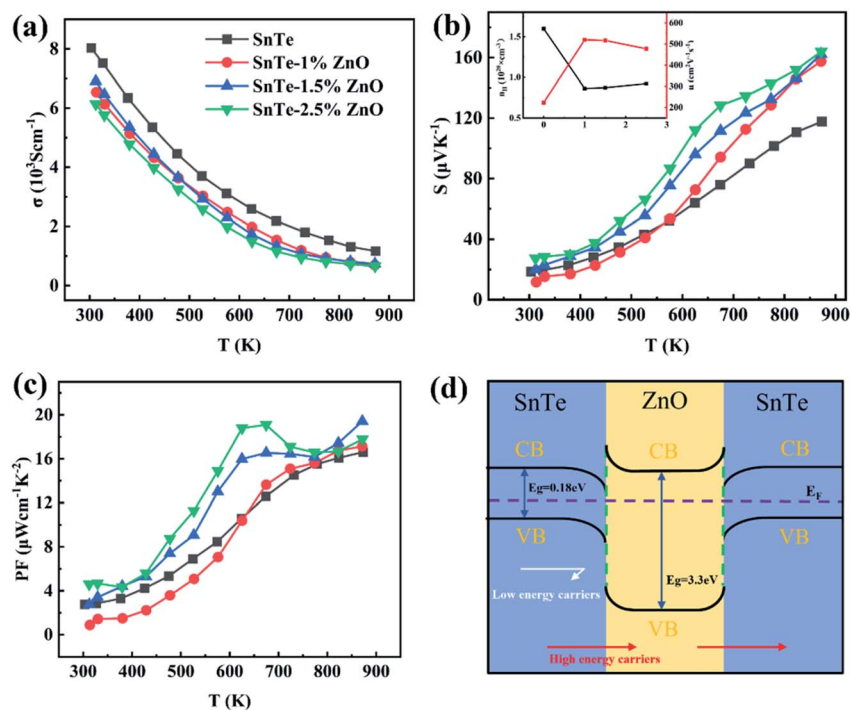


Fig. 7 Electrical properties: (a) electrical conductivity, (b) Seebeck coefficient, and (c) power factor, as a function of temperature for SnTe– $x\%$  ZnO. (d) Schematic diagram of the carrier energy barrier at the heterogeneous interface of SnTe/ZnO core/shell; the inset graph of (b) shows the hole concentration and the carrier mobility of SnTe– $x\%$  ZnO at room temperature.



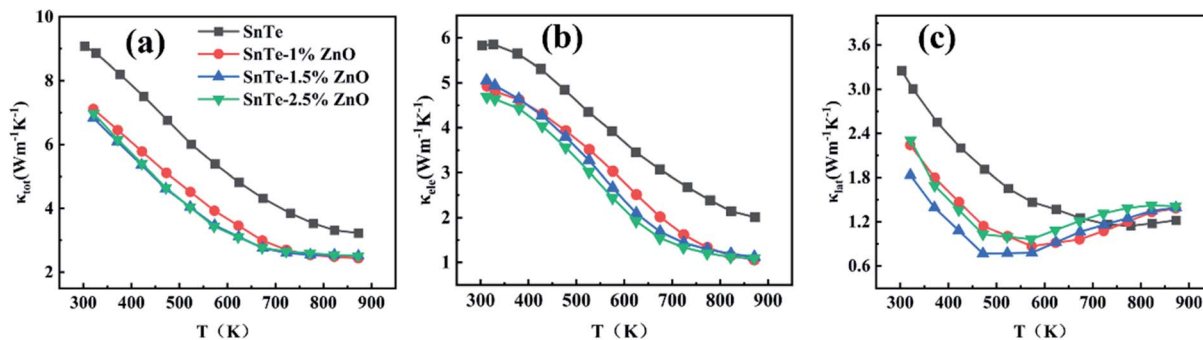


Fig. 8 Thermal properties: (a) thermal conductivity, (b) electronic thermal conductivity, (c) lattice thermal conductivity as a function of temperature for SnTe- $x\%$  ZnO samples.

restraining the diffusion/drift of carriers with energy  $E$  lower than the barrier height  $V_b$ .<sup>29</sup> Thus, the lower energy carriers will be filtered and high energy carriers will cross the energy barrier. Meanwhile, the average energy of carriers will be increased, which contributes to the increased  $\mu$ .<sup>30,39,40</sup> Moreover, the  $\mu$  decreases slightly with the increasing ZnO content, which is opposite to that of  $n_H$ .

It can be obviously observed in Fig. 7b that the  $S$  of all the samples is positive, indicating p-type conduction. The  $S$  of SnTe- $x\%$  ZnO ( $x = 1, 1.5, 2.5$ ) samples is higher than the pristine SnTe when  $T > 573$  K. For example, the  $S$  of the pristine SnTe increases from  $18.55 \mu\text{W cm}^{-1} \text{K}^{-2}$  at 300 K to  $117.79 \mu\text{W cm}^{-1} \text{K}^{-2}$  at 873 K while the  $S$  of SnTe-1.5% ZnO increases from  $22.98 \mu\text{W cm}^{-1} \text{K}^{-2}$  at 300 K to  $162.25 \mu\text{W cm}^{-1} \text{K}^{-2}$  at 873 K. Furthermore, the  $S$  increases with the increasing ZnO content, which is contrary to  $\sigma$ . The improvement of  $S$  can be attributed to the energy filtering effect caused by the SnTe/ZnO heterogeneous interface.<sup>31</sup> The energy barrier can not only get the high energy carriers across but also filter low energy carriers, finally leading to the increased carrier effective mass  $m^*$ .<sup>41</sup> Thus, the  $S$  can be improved simultaneously. Due to the enhancement of  $S$ , the power factor PF of SnTe- $x\%$  ZnO samples is effectively improved as shown in Fig. 7c, and a maximum PF of  $19.42 \mu\text{W cm}^{-1} \text{K}^{-2}$  at 873 K is obtained in SnTe-1.5% ZnO.

Fig. 8a shows the temperature-dependent total thermal conductivity  $\kappa$  for SnTe- $x\%$  ZnO ( $x = 0, 1, 1.5, 2.5$ ) samples. The  $\kappa$  of all the samples decreases with the increase of temperature monotonously. Meanwhile, the  $\kappa$  drops sharply in the low/moderate temperature region but the tendency slows down in the high temperature region.<sup>42,43</sup> The  $\kappa$  decreases remarkably after constructing SnTe/ZnO core-shell structure because of the simultaneous decrease of  $\kappa_e$  and  $\kappa_l$ . For instance,  $\kappa$  at the room temperature drops sharply to  $6.83 \text{ W m}^{-1} \text{K}^{-1}$  of SnTe-1.5% ZnO, which is 29.7% lower than the pristine SnTe. The electrical thermal conductivity  $\kappa_e$  (Fig. 8b) is calculated by the formula:  $\kappa_e = L\sigma T$ . The  $\kappa_e$  experiences a sharp slump compared with the pristine SnTe and is in a downward trend with the increasing temperature. The decreasing tendency of the  $\kappa_e$  slows down in the high temperature region, which is of positive relevance with that of  $\sigma$ .

Fig. 8c shows the lattice thermal conductivity  $\kappa_l$  as a function of temperature for SnTe- $x\%$  ZnO ( $x = 0, 1, 1.5, 2.5$ ) samples.

The  $\kappa_l$  of SnTe- $x\%$  ZnO ( $x = 1, 1.5, 2.5$ ) samples is dramatically lower than that of the SnTe below 673 K. For instance, the  $\kappa_l$  of SnTe-1.5% ZnO is  $1.83 \text{ W m}^{-1} \text{K}^{-1}$  at room temperature, which is 43.7% lower than the pristine SnTe. However, the  $\kappa_l$  of all ZnO-incorporated samples is higher than pristine SnTe when the temperature is over 673 K. Because the density of interface caused by SnTe/ZnO core-shell structure can only scatter low/medium frequency phonons and thus reduce  $\kappa_l$  in the low/medium temperature region.<sup>33,44</sup> The heat transfer of high frequency phonons is dominated at high temperatures, so the effect of interfaces is weakened.<sup>43,45</sup>

Based on the results of thermal performance and electrical performance, the dimensionless figure of merit ( $ZT$ ) can be obtained by utilizing the formula:  $ZT = S^2\sigma T/\kappa$ . Fig. 9 shows temperature dependence of  $ZT$  values for SnTe- $x\%$  ZnO ( $x = 0, 1, 1.5, 2.5$ ) samples. Benefiting from simultaneously optimized PF and  $\kappa$ , a maximum  $ZT$  value of 0.67 is achieved in SnTe-1.5% ZnO at 873 K, which is 50% higher than pristine SnTe. Nevertheless, the minimum  $\kappa_l$  of SnTe- $x\%$  ZnO ( $\sim 1.83 \text{ W m}^{-1} \text{K}^{-1}$ ) is far higher than the amorphous limit of SnTe ( $\sim 0.40 \text{ W m}^{-1} \text{K}^{-1}$ ), motivating us to reduce  $\kappa_l$  by applying the other strategy.

To further improve the thermoelectric performance, we try to introduce massive point defects, including substitutional and interstitial defects to regulate the thermal performance of high temperature ends.<sup>46</sup> Here, 3–6% mol of  $\text{Cu}_2\text{Te}$  is chosen and alloyed with SnTe matrix to further reduce  $\kappa_l$ . Fig. 10a and

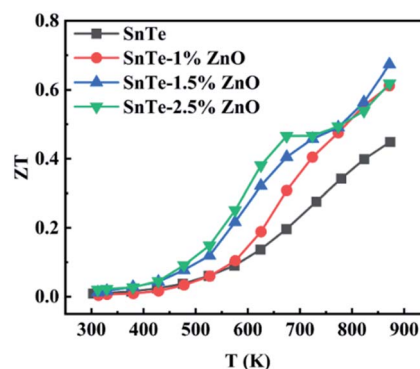


Fig. 9 Temperature dependence of  $ZT$  values for SnTe- $x\%$  ZnO.



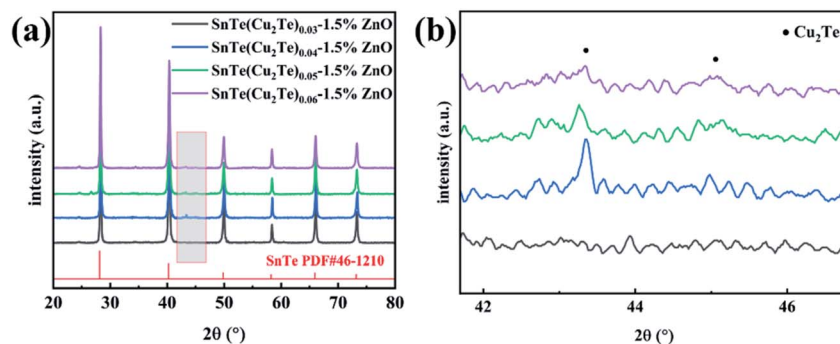


Fig. 10 (a) XRD patterns of  $\text{SnTe}(\text{Cu}_2\text{Te})_y-1.5\% \text{ZnO}$  ( $y = 0.03, 0.04, 0.05, 0.06$ ) bulks. (b)  $2\theta$  shifts for  $\text{SnTe}(\text{Cu}_2\text{Te})_y-1.5\% \text{ZnO}$  ( $y = 0.03, 0.04, 0.05, 0.06$ ) bulks.

b displays the XRD pattern of  $\text{SnTe}(\text{Cu}_2\text{Te})_y-1.5\% \text{ZnO}$  ( $y = 0.03, 0.04, 0.05, 0.06$ ) bulks, the characteristic peaks can be indexed to rock-salt  $\text{SnTe}$  ( $Fm\bar{3}m$ ) structure. However, the  $\text{Cu}_2\text{Te}$

diffraction peak can be detected when the  $\text{Cu}_2\text{Te}$  content is over 0.03. For  $y = 0.03$  sample,  $\text{Cu}_2\text{Te}$  peaks cannot be detected by XRD measurements due to its low content.

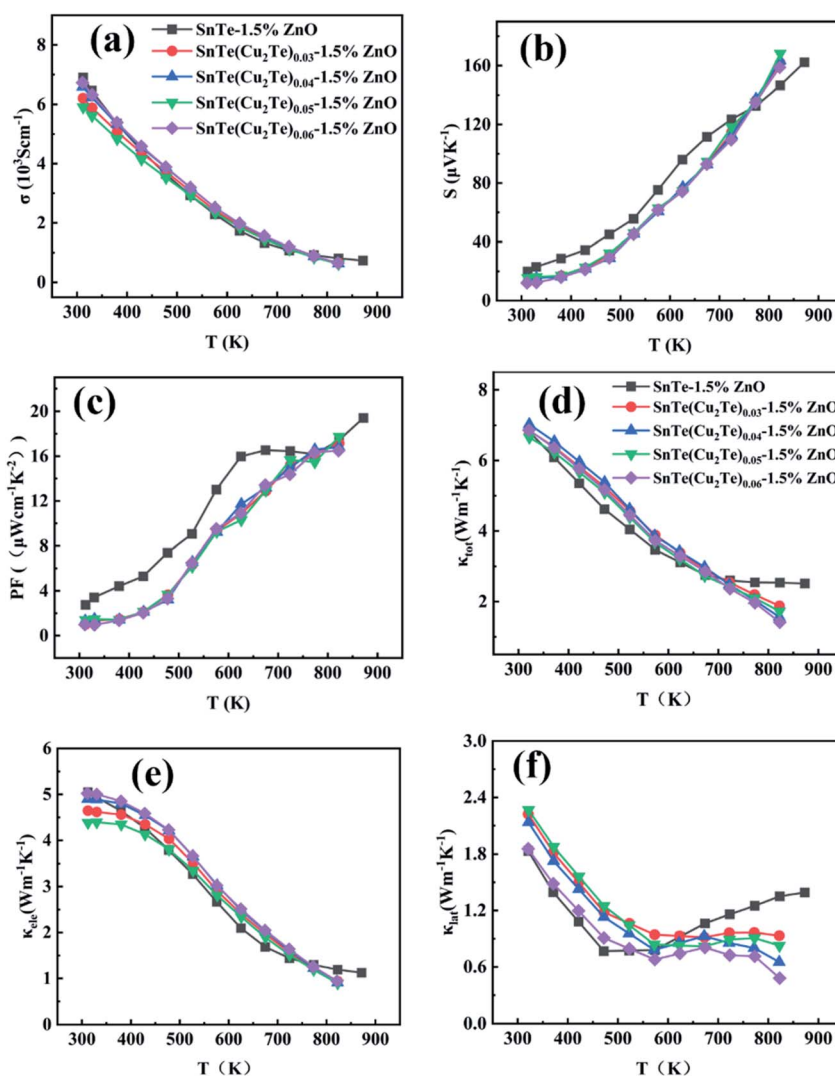


Fig. 11 Electrical properties: (a) electrical conductivity, (b) Seebeck coefficient, and (c) power factor, as a function of temperature  $\text{SnTe}(\text{Cu}_2\text{Te})_y-1.5\% \text{ZnO}$ . Thermal properties: (d) thermal conductivity, (e) electronic thermal conductivity, (f) lattice thermal conductivity as a function of temperature for  $\text{SnTe}(\text{Cu}_2\text{Te})_y-1.5\% \text{ZnO}$  samples.



The measurement temperature of thermoelectrical performance for SnTe(Cu<sub>2</sub>Te)<sub>y</sub>-1.5% ZnO (Fig. 11) is range from 300 K to 823 K, avoiding the deformation of samples above 823 K. Fig. 11a–c shows the temperature dependence of  $\sigma$ ,  $S$ , and PF of SnTe(Cu<sub>2</sub>Te)<sub>y</sub>-1.5% ZnO samples. It is clearly observed in Fig. 11a that the  $\sigma$  drops slightly over the entire temperature region after Cu<sub>2</sub>Te alloying. As can be seen in Fig. 11b, Cu<sub>2</sub>Te-alloying samples exhibit a lower  $S$  when compared with Cu<sub>2</sub>Te-free sample in the low/medium temperature region, but exhibits a higher  $S$  at the high temperature end. Thus a peak  $S$  of 168.21 mV K<sup>-1</sup> at 823 K was obtained for SnTe(Cu<sub>2</sub>Te)<sub>0.05</sub>-1.5% ZnO. The simultaneous decreasing of  $\sigma$  and  $S$  contributes to the degradation of PF (Fig. 11c) in the low/medium temperature region. However, in the high temperature region, the PF of Cu<sub>2</sub>Te-alloying samples is comparable to that of SnTe-1.5% ZnO, which is attributed to the fact that the enhancement of  $S$  compensates for the reduction of  $\sigma$ .

Fig. 11d–f shows temperature dependence of  $\kappa$ ,  $\kappa_e$ , and  $\kappa_1$  of SnTe(Cu<sub>2</sub>Te)<sub>y</sub>-1.5% ZnO samples. In Fig. 11d, the  $\kappa$  of Cu-alloying samples drops sharply in the high temperature region when compared with SnTe-1.5% ZnO, reaching the bottom of 1.42 W m<sup>-1</sup> K<sup>-1</sup> for SnTe(Cu<sub>2</sub>Te)<sub>0.06</sub>-1.5% ZnO at 823 K. The  $\kappa_e$  (Fig. 11e) of Cu<sub>2</sub>Te-alloying samples drops sharply at the high temperature end, comparing with the SnTe-1.5% ZnO sample. Fig. 11f indicates that the  $\kappa_1$  of Cu<sub>2</sub>Te-alloying samples decreases effectively above 600 K when compared with SnTe-1.5% ZnO, and the SnTe(Cu<sub>2</sub>Te)<sub>0.06</sub>-1.5% ZnO sample reaches the lowest  $\kappa_1$  of 0.48 W m<sup>-1</sup> K<sup>-1</sup> at 823 K, closing to the amorphous limit of SnTe.<sup>47</sup> It is because the point defects *via* Cu<sub>2</sub>Te-alloying, including substitutional and interstitial defects, produce local mass and strain fluctuations in the matrix, which can scatter the high frequency phonons effectively.<sup>46,48</sup>

Fig. 12 displays temperature dependence of  $ZT$  values for the pristine SnTe and SnTe(Cu<sub>2</sub>Te)<sub>y</sub>-1.5% ZnO ( $y = 0, 0.03, 0.04, 0.05, 0.06$ ) samples. The  $ZT$  value first increases from 0.45 in SnTe to 0.67 in SnTe-1.5% ZnO at 873 K after constructing SnTe/ZnO core-shell structure, and further increases through alloying SnTe matrix with Cu<sub>2</sub>Te, reaching the peak of  $\sim 0.94$  in SnTe(Cu<sub>2</sub>Te)<sub>0.06</sub>-1.5% ZnO at 823 K.

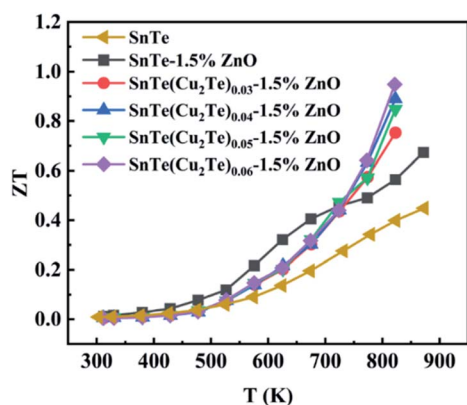


Fig. 12 Temperature dependence of  $ZT$  values for the pristine SnTe and SnTe(Cu<sub>2</sub>Te)<sub>y</sub>-1.5% ZnO samples.

## 4. Conclusion

To sum up, a facile hydrothermal method is applied to *in situ* synthesize SnTe/ZnO core-shell particles. The energy filtering effect constructed by SnTe/ZnO core-shell structure significantly reduces the carrier concentration and improves the Hall mobility, finally leading to a peak power factor of 19.42  $\mu\text{W cm}^{-1} \text{K}^{-2}$  for SnTe-1.5% ZnO at 873 K. Besides, the interfaces introduced by ZnO intensely scatter the low/medium frequency phonons, and a mass of point defects involved through Cu<sub>2</sub>Te-alloying strength the scattering of high frequency phonons successfully, which contributes to the lowest  $\kappa_1$  of 0.48 W m<sup>-1</sup> K<sup>-1</sup> in this work, closing to the amorphous limit. Finally, a peak  $ZT$  of 0.94 is achieved in SnTe(Cu<sub>2</sub>Te)<sub>0.06</sub>-1.5% ZnO at 823 K, which is 138% higher than that for the pristine SnTe. This work shows the feasibility of improving the TE performance by *in situ* synthesizing ZnO core-shell structure, and also has a referential value for other thermoelectric materials.

## Conflicts of interest

The authors declare that they have no known competing financial interests or personal relationships that could have appeared to influence the work reported in this paper.

## Acknowledgements

This work was supported by the National Natural Science Foundation of China (No. 52101220) and the Fundamental Research Funds for the Central Universities (JZ2021HGTA0155, JZ2021HGQA0189).

## References

- 1 F. J. Disalvo, *Science*, 1999, **285**, 703–706.
- 2 R. Moshwan, L. Yang, J. Zou and Z. G. Chen, *Adv. Funct. Mater.*, 2017, **27**, 1703278.
- 3 J. W. Zhang, Z. W. Wu, F.-P. Zhang, X. Y. Yang and J. X. Zhang, *J. Electron. Mater.*, 2021, **50**, 649–656.
- 4 Y. Wang, L. Yang, X. L. Shi, X. Shi, L. Chen, M. S. Dargusch, J. Zou and Z. G. Chen, *Adv. Mater.*, 2019, **31**, 1807916.
- 5 L. Yang, Z. G. Chen, M. S. Dargusch and J. Zou, *Adv. Energy Mater.*, 2018, **8**, 1701797.
- 6 Z. Chen, J. Li, J. Tang, F. Zhang, Y. Zhong, H. Liu and R. Ang, *J. Mater. Sci. Technol.*, 2021, **89**, 45–51.
- 7 Y. Luo, S. Cai, S. Hao, F. Pielnhöfer, I. Hadar, Z. Z. Luo, J. Xu, C. Wolverton, V. P. Dravid, A. Pfitzner, Q. Yan and M. G. Kanatzidis, *Joule*, 2020, **4**, 159–175.
- 8 Y. Luo, Z. Ma, S. Hao, S. Cai, Z. Z. Luo, C. Wolverton, V. P. Dravid, J. Yang, Q. Yan and M. G. Kanatzidis, *J. Am. Chem. Soc.*, 2022, **144**, 1445–1454.
- 9 Z. Bu, X. Zhang, B. Shan, J. Tang, H. Liu, Z. Chen, S. Lin, W. Li and Y. Pei, *Sci. Adv.*, 2021, **7**, eabf2738.
- 10 Y. Luo, T. Xu, Z. Ma, D. Zhang, Z. Guo, Q. Jiang, J. Yang, Q. Yan and M. G. Kanatzidis, *J. Am. Chem. Soc.*, 2021, **143**, 13990–13998.



- 11 K. Imasato, C. Fu, Y. Pan, M. Wood, J. J. Kuo, C. Felser and G. J. Snyder, *Adv. Mater.*, 2020, **32**, 1908218.
- 12 L. Su, D. Wang, S. Wang, B. Qin, Y. Wang, Y. Qin, Y. Jin, C. Chang and L. D. Zhao, *Science*, 2022, **375**, 1385–1389.
- 13 S. Liu, Y. Yu, D. Wu, X. Xu, L. Xie, X. Chao, M. Bosman, S. J. Pennycook, Z. Yang and J. He, *Adv. Funct. Mater.*, 2021, **31**, 2007340.
- 14 V. Prokopiv, M. O. Galushchak, I. V. Horichok, T. Parashchuk, O. Matkivskiy, V. V. Bachuk and R. O. Dzumedzey, *Phys. Chem. Solid State*, 2019, **20**, 149–155.
- 15 G. Tan, L. D. Zhao, F. Shi, J. W. Doak, S. H. Lo, H. Sun, C. Wolverton, V. P. Dravid, C. Uher and M. G. Kanatzidis, *J. Am. Chem. Soc.*, 2014, **136**, 7006–7017.
- 16 W. Li, Y. Wu, S. Lin, Z. Chen, J. Li, X. Zhang, L. Zheng and Y. Pei, *ACS Energy Lett.*, 2017, **2**, 2349–2355.
- 17 M. Zhou, Z. M. Gibbs, H. Wang, Y. Han, C. Xin, L. Li and G. J. Snyder, *Phys. Chem. Chem. Phys.*, 2014, **16**, 20741–20748.
- 18 J. D. I. Masek and D. Nuzhnyj, *Acta Phys. Pol.*, 1997, **92**, 915–918.
- 19 X. Dong, W. Cui, W. D. Liu, S. Zheng, L. Gao, L. Yue, Y. Wu, B. Wang, Z. Zhang, L. Chen and Z. G. Chen, *J. Mater. Sci. Technol.*, 2021, **86**, 204–209.
- 20 D. G. Cahill, S. K. Watson and R. O. Pohl, *Phys. Rev. B*, 1992, **46**, 6131–6140.
- 21 A. Banik, U. Shenoy, S. Anand, U. Waghmare and K. Biswas, *Chem. Mater.*, 2014, **27**, 581–587.
- 22 G. Tan, F. Shi, J. W. Doak, H. Sun, L. D. Zhao, P. Wang, C. Uher, C. Wolverton, V. P. Dravid and M. G. Kanatzidis, *Energy Environ. Sci.*, 2015, **8**, 267–277.
- 23 G. Tan, F. Shi, S. Hao, H. Chi, L. D. Zhao, C. Uher, C. Wolverton, V. P. Dravid and M. G. Kanatzidis, *J. Am. Chem. Soc.*, 2015, **137**, 5100–5112.
- 24 J. He, X. Tan, J. Xu, G. Q. Liu, H. Shao, Y. Fu, X. Wang, Z. Liu, J. Xu, H. Jiang and J. Jiang, *J. Mater. Chem. A*, 2015, **3**, 19974–19979.
- 25 H. Deng, X. Lou, W. Lu, J. Zhang, D. Li, S. Li, Q. Zhang, X. Zhang, X. Chen, D. Zhang, Y. Zhang and G. Tang, *Nano Energy*, 2021, **81**, 105649.
- 26 K. Biswas, J. He, G. Wang, S. H. Lo, C. Uher, V. P. Dravid and M. G. Kanatzidis, *Energy Environ. Sci.*, 2011, **4**, 4675–4684.
- 27 Q. Zhang, B. Liao, Y. Lan, K. Lukas, W. Liu, K. Esfarjani, C. Opeil, D. Broido, G. Chen and Z. Ren, *Proc. Natl. Acad. Sci. U. S. A.*, 2013, **110**, 13261–13266.
- 28 M. Bachmann, M. Czerner and C. Heiliger, *Phys. Rev. B*, 2012, **86**, 115320.
- 29 D. Narducci, S. Frabboni and X. Zianni, *J. Mater. Chem. C*, 2015, **3**, 12176–12185.
- 30 Z. Ma, C. Wang, J. Lei, D. Zhang, Y. Chen, Y. Wang, J. Wang and Z. Cheng, *Nanoscale*, 2020, **12**, 26.
- 31 Z. Zhou, J. Yang, Q. Jiang, D. Zhang, J. Xin, X. Li, Y. Ren and X. He, *J. Am. Ceram. Soc.*, 2017, **100**, 5723–5730.
- 32 J. Zhang, S. Li, Z. Zhu, Z. Wu and J. Zhang, *Dalton Trans.*, 2021, **50**, 10515–10523.
- 33 J. Zhang, S. Li, Z. Wu and J. Zhang, *J. Alloys Compd.*, 2021, **889**, 161651.
- 34 Z. Wang, B. Cheng, L. Zhang, J. Yu and H. Tan, *Sol. RRL*, 2022, **6**, 2100587.
- 35 J. Li, T. Zhang, C. Han, H. Li, R. Shi, J. Tong and B. Li, *J. Mater. Chem. A*, 2019, **7**, 455–460.
- 36 Z. H. Zhang, Z. F. Liu, J. F. Lu, X. B. Shen, F. C. Wang and Y. D. Wang, *Scr. Mater.*, 2014, **81**, 56–59.
- 37 S. Li, J. Xin, A. Basit, Q. Long, S. Li, Q. Jiang, Y. Luo and J. Yang, *Adv. Sci.*, 2020, **7**, 1903493.
- 38 K. C. Kim, S.-S. Lim, S. H. Lee, J. Hong, D. Y. Cho, A. Y. Mohamed, C. M. Koo, S. H. Baek, J. S. Kim and S. K. Kim, *ACS Nano*, 2019, **13**, 7146–7154.
- 39 Z. Ma, C. Wang, Y. Chen, L. Li, S. Li, J. Wang and H. Zhao, *Mater. Today Phys.*, 2021, **17**, 100350.
- 40 L. Fu, J. Yang, J. Peng, Q. Jiang, Y. Xiao, Y. Luo, D. Zhang, Z. Zhou, M. Zhang, Y. Cheng and F. Cheng, *J. Mater. Chem. A*, 2015, **3**, 1010–1016.
- 41 T. Hong, C. Guo, D. Wang, B. Qin, C. Chang, X. Gao and L. D. Zhao, *Mater. Today Energy*, 2022, **25**, 100985.
- 42 S. K. Kihoi, U. S. Shenoy, J. N. Kahi, H. Kim, D. K. Bhat and H. S. Lee, *ACS Sustainable Chem. Eng.*, 2022, **10**, 1367–1372.
- 43 Y. Pei and D. T. Morelli, *Appl. Phys. Lett.*, 2009, **94**, 122112.
- 44 X. Zhang, Y. Zhou, Y. Pei, Y. Chen, B. Yuan, S. Zhang, Y. Deng, S. Gong, J. He and L. D. Zhao, *J. Alloys Compd.*, 2017, **709**, 575–580.
- 45 Z. Chen, B. Ge, W. Li, S. Lin, J. Shen, Y. Chang, R. Hanus, G. J. Snyder and Y. Pei, *Nat. Commun.*, 2017, **8**, 13828.
- 46 Y. Pei, L. Zheng, W. Li, S. Lin, Z. Chen, Y. Wang, X. Xu, H. Yu, Y. Chen and B. Ge, *Adv. Electron. Mater.*, 2016, **2**, 1600019.
- 47 J. W. Zhang, Z. W. Wu, B. Xiang, N. N. Zhou, J. L. Shi and J. X. Zhang, *ACS Appl. Mater. Interfaces*, 2020, **12**, 21863–21870.
- 48 F. Guo, B. Cui, H. Geng, Y. Zhang, H. Wu, Q. Zhang, B. Yu, S. J. Pennycook, W. Cai and J. Sui, *Small*, 2019, **15**, 1902493.

